energies

MDPI

Article

Air-Gap-Domain Topology Optimization for Electromagnetic Vibration and Noise Reduction in an Interior Permanent-Magnet Motor

Jiqi Wu [1,*], Jingwen Xu [1], Zixuan Xiang [1], Peng Zhao [1] and Tengfei Song [2]

[1] School of Electrical and Information Engineering, Jiangsu University, Zhenjiang 212013, China; 2212507040@stmail.ujs.cn (J.X.); zxxiang@ujs.edu.cn (Z.X.); 2212307041@stmail.ujs.edu.cn (P.Z.)
[2] Suzhou Inovance Automotive Co., Ltd., Suzhou 212013, China; songtengfei@inovance.com
* Correspondence: wjq@ujs.edu.cn

Abstract

Electromagnetic vibration and noise become increasingly pronounced in high-power-density traction motors. This paper proposes harmonic-guided air-gap-domain topology optimization for a 48-slot, eight-pole interior permanent-magnet motor with hairpin windings. A normalized Gaussian network is used to parameterize the rotor-edge topology. NSGA-II then optimizes the network weights to adjust the characteristic flux-density harmonics in the air-gap-domain at the low-speed high-load (OC1) and high-speed light-load (OC2) operating points, while meeting torque, stress, and manufacturability requirements. Multiphysics simulations show a 57.52% reduction in $F_r(48, 12f)$ at OC1. The $12f$ vibration acceleration decreases by 86.30% and 56.65% at OC1 and OC2, respectively, while the maximum sound-pressure level on the evaluation surface decreases by 1.04 and 1.75 dB. Average torque remains comparable to the baseline. Finally, a 40 kW prototype is tested to evaluate electromagnetic performance and vibration and noise characteristics.

Keywords: interior permanent-magnet motor; electromagnetic vibration and noise; multi-objective optimization; topology optimization

1. Introduction

As the global energy transition and the electrification of automobiles continue to accelerate, the drive motor has become a key component that determines the efficiency, dynamic performance, and ride comfort of electric vehicles [1]. Permanent-magnet synchronous motors (PMSMs), due to their high torque density, high efficiency, compact design, and strong weak-field acceleration capability, are widely used in electric vehicle traction systems [2,3]. However, as motor power density and speed ranges continue to increase, the electromagnetic vibrations and noise generated by drive motors have become more pronounced, directly affecting the vehicle's ride comfort and the operational reliability of the motor system [4]. Therefore, research into the vibration and noise characteristics of high-power-density permanent-magnet motors holds significant engineering importance [5].

The sources of vibration and noise in permanent-magnet motors are relatively complex and typically include various factors such as mechanical, electromagnetic, and aerodynamic causes [6]. Among these, mechanical vibration and noise are primarily caused by bearing defects, rotor imbalance, assembly deviations, and transmission system coupling; aerodynamic noise, on the other hand, is related to cooling fans, airflow disturbances,

Check for updates

Academic Editor: Alessandro Niccolai

Received: 27 August 2026
Revised: 26 October 2026
Accepted: 27 October 2026
Published: 3 November 2026

Copyright: © 2026 by the authors. Licensee MDPI, Basel, Switzerland. This article is an open access article distributed under the terms and conditions of the Creative Commons Attribution (CC BY) license.

and ventilation structures [7]. In contrast, electromagnetic vibration and noise are closely related to the motor's electromagnetic design and operating conditions, and constitute the primary component of vibration and noise in most permanent-magnet motors [8]. Electromagnetic vibration is primarily caused by harmonics in the air-gap magnetic field. Factors such as the magnetic force of permanent magnets, armature reaction, stator slots, magnetic circuit saturation, and inverter current harmonics generate spatial and temporal harmonics in the air-gap magnetic flux density. When these harmonics interact, they form radial and tangential electromagnetic force waves of different orders and frequencies [9]. Radial force waves act on the stator teeth and yoke, causing elastic deformation of the stator and motor housing and radiating noise outward; tangential force waves primarily manifest as torque ripple and may further induce torsional vibrations or structure-borne noise through the rotor, shaft system, and mounting structure [10–12].

To address the issues of electromagnetic vibration and noise in permanent-magnet motors, scholars both domestically and internationally have proposed various suppression methods focused on two aspects: attenuating excitation sources and regulating structural responses. Zhou et al. proposed a low-vibration design method targeting radial electromagnetic force harmonics, treating radial force harmonics as a bridge between the electromagnetic field and structural vibration, and achieving vibration suppression through the transfer of the lowest nonzero spatial order on the stator side and the attenuation of dominant harmonic amplitudes on the rotor side [13]. Xing et al. optimized the stator slot parameters of a permanent-magnet synchronous motor and combined deep neural networks with an immune cloning algorithm to attenuate key electromagnetic force waves, thereby reducing the maximum vibration acceleration of the prototype under no-load and rated load conditions, respectively [14]. Shen et al. established analytical models of radial and tangential electromagnetic force waves for a fractional-slot concentrated-winding, interior permanent-magnet synchronous motor, effectively reducing electromagnetic vibration and noise [15]. Ma et al. used resonance controllers to suppress fifth- and seventh-order current harmonics, thereby reducing vibration and noise in permanent-magnet motors [16]. In summary, motor vibration typically requires the suppression of specific-order forces in the stator and rotor. Existing methods adjust these specific-order forces by modifying the motor structure or altering the excitation current; however, given design requirements such as torque and efficiency, it is difficult to achieve a low-vibration, low-noise motor structure that optimally balances multiple objectives [17–19].

In recent years, intelligent optimization algorithms and topology optimization techniques have provided new approaches for optimizing the vibration and noise design of electric motors. Yao et al. proposed a method for rapid prediction and staged optimization of electromagnetic vibration in permanent-magnet synchronous motors, considering vibration, torque, and efficiency in a multi-objective optimization framework [18]. Zhang et al. proposed a multi-objective optimization method for IPMSM noise based on a nonuniform air-gap micro-slot structure, which reduced back-EMF harmonics, torque ripple, and 24th- and 48th-order vibration responses [20]. Li et al. proposed a rotor structure with a single pole-pair double-layer permanent-magnet shift to reduce torque ripple and vibration in a delta-type IPMSM [21]. Sato et al. applied a normalized Gaussian network (NGnet) to multimaterial topology optimization of electric machines [22]. Kim and Lim optimized IPMSM rotor flux barriers using NGnet [23], while Takenouchi et al. combined topology and parameter optimization with mechanical-strength constraints [24]. Multi-objective optimization has become an effective means of improving motor vibration and noise by balancing electromagnetic, mechanical, and acoustic performance. However, as motors are increasingly required to meet performance demands across multiple operating conditions, the design must account for condition-dependent force harmonics and competing targets.

Adjusting conventional structural parameters alone may not provide sufficient flexibility to satisfy these complex multi-condition requirements.

To address this challenge, this paper proposes an NGnet-guided air-gap topology optimization method for a 48-slot, eight-pole interior permanent-magnet motor. The method coordinates different electromagnetic force-wave targets under multiple operating conditions. NGnet provides flexible control of the rotor-edge contour, enabling finer air-gap design to balance the motor's torque and vibration characteristics across multiple operating conditions. The rest of this paper is organized as follows: The mechanisms of electromagnetic vibration and noise generation in permanent-magnet motors with hairpin windings are systematically analyzed, the formation process of radial electromagnetic force waves is elucidated, and the basic approach for suppressing electromagnetic excitation through air-gap-domain optimization is introduced in Section 2. In Section 3, a multi-operating-condition air-gap optimization model is established, a normalized Gaussian network is used to describe the local topology of the air gap, and the NSGA-II algorithm is adopted to obtain the final optimized structure. In Section 4, the optimization results are validated, with emphasis on the comparison of vibration and noise performance before and after optimization. Section 5 presents prototype fabrication and experimental testing. Conclusions are drawn in Section 6.

2. Vibration and Noise Mechanisms of the Interior Permanent-Magnet Motor

2.1. Electromagnetic Vibration and Noise Mechanism

During operation, the air-gap magnetic field produces periodic electromagnetic forces on the stator teeth and yoke. These forces contribute to torque production and excite the stator core and housing. Strong vibration occurs when the spatial order and temporal frequency of a force wave couple with a structural mode. The vibrating housing then radiates electromagnetic noise. Figure 1 summarizes this process. Motor topology, inverter current harmonics, winding parameters, air-gap nonuniformity, and load variation make the air-gap flux density nonsinusoidal. It therefore contains harmonics with different spatial orders and temporal frequencies. Nonlinear coupling among these harmonics produces the electromagnetic excitation force.

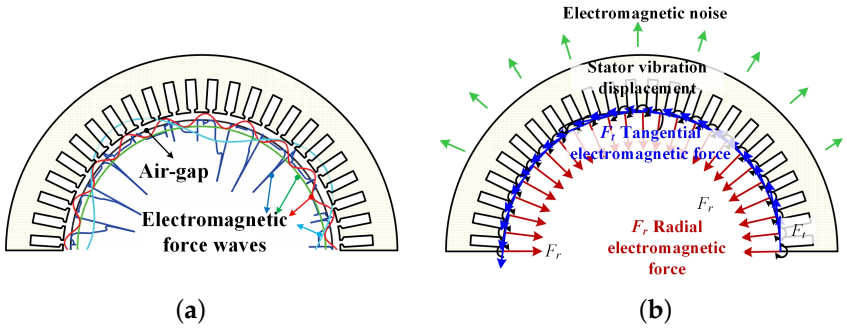


Figure 1. Mechanism of electromagnetic vibration and noise in the motor: (**a**) spatial force harmonics in the air gap; and (**b**) equivalent tooth-tip forces and moments.

The air-gap force has tangential and radial components. The tangential component is associated with torque, torque ripple, and tooth rocking. The radial component acts normal to the tooth surface and deforms the stator. This vibration reaches the housing and disturbs the surrounding air. A strong resonant response occurs only when the spatial and temporal characteristics of the excitation match a structural mode. The modal resonance amplification factor k_m quantifies this effect:

$$k_m = \frac{1}{\sqrt{\left[1 - \left(\frac{f_r}{f_m}\right)^2\right]^2 + \left[2\zeta_m\left(\frac{f_r}{f_m}\right)\right]^2}} \tag{1}$$

where f_r is the excitation frequency, f_m is the structural natural frequency, and ζ_m is the modal damping ratio. When f_r approaches f_m, k_m rises sharply and amplifies the structural response. Resonance is therefore a major cause of electromagnetic vibration and noise. The stator can also be approximated as a thin cylindrical shell. If asymmetric excitation is neglected, its static displacement and vibration acceleration are

$$Y_0 = \frac{R_i R_y}{E h_y} p_0 \tag{2}$$

$$Y_m\,(m \geq 2) = \frac{12 R_i R_y^3}{E h_y^3}\left(\frac{1}{m^2 - 1}\right)^2 p_m \tag{3}$$

$$A_m = Y_m \omega_{\text{exc}}^2 = Y_m (2\pi f_r)^2 \tag{4}$$

where $\omega_{\text{exc}} = 2\pi f_r$ is the angular frequency of the electromagnetic excitation, where m is the spatial order of the radial pressure, p_m is its amplitude, and Y_m is the peak displacement. R_i is the inner radius of the stator yoke, R_y is its mean radius, E is Young's modulus, and h_y is the radial thickness of the yoke.

Equations (2) and (3) show that the fourth-order term in the denominator suppresses the response when $m \geq 2$. In integer-slot motors with many poles, the zeroth-order force wave can therefore dominate the lowest nonzero-order waves. Vibration control should focus on the zeroth-order radial component.

2.2. Calculation and Analysis of Electromagnetic Vibration and Noise

The previous section identified low-order radial force waves as the main excitation source. This section derives their spatial orders and frequencies from the coupling of magnetomotive force (MMF) and air-gap permeance. The results guide the subsequent structural optimization. The force-wave spectrum is determined by the stator armature MMF, the rotor permanent-magnet MMF, and slot-induced air-gap permeance. Their modulation produces radial excitations with specific spatial orders and rotational frequencies. These excitations act on the tooth tips and drive the stator core and housing. The fundamental armature MMF is

$$F_1 = \frac{3}{2} F_{m1} = \frac{3}{2} \frac{2\sqrt{2}}{\pi} \frac{N k_{w1}}{p} I \approx 1.35 \frac{N k_{w1}}{p} I \tag{5}$$

where k_{w1} is the winding factor of the fundamental MMF and N is the number of series turns per phase. The permanent-magnet MMF is

$$f_{\text{pm}}(\theta, t) = \sum_{\mu} F_\mu \cos(\mu\omega t - \mu p\theta), \quad \mu = 2k + 1, \quad k = 0, 1, 2, \ldots \tag{6}$$

where F_μ is the amplitude of the μth rotor MMF harmonic and μ is its harmonic order. With stator slotting, the air-gap permeance is

$$\Lambda(\theta, t) = \Lambda_0 + \sum_{k=1}^{\infty} \Lambda_k \cos(kZ\theta) \tag{7}$$

where Z is the number of stator slots, Λ_0 is the mean permeance per unit air-gap area, and Λ_k is the kth slotting permeance harmonic. The radial electromagnetic force is

$$F_r(\theta,t) = \frac{1}{2\mu_0}\left[B_r^2(\theta,t) - B_t^2(\theta,t)\right] \approx \frac{1}{2\mu_0}B_r^2(\theta,t) \tag{8}$$

where μ_0 is the permeability of free space. The tangential flux density $B_t(\theta,t)$ is much smaller than the radial component $B_r(\theta,t)$ except near the tooth edges. The air-gap flux density $B(\theta,t)$ is the product of the MMF $f(\theta,t)$ and the permeance $\Lambda(\theta,t)$. If air-gap saturation is neglected, the total flux density is

$$B(\theta,t) = \left[f_{\mathrm{pm}}(\theta,t) + f_{\mathrm{arm}}(\theta,t)\right]\Lambda(\theta,t) \tag{9}$$

Substitution of Equations (5)–(7) and (9) into Equation (8) gives

$$F_r(\theta,t) = \sum_r F_r \cos(\omega_r t - r\theta + \varphi_r) \tag{10}$$

where r is the spatial order, ω_r is the angular frequency, and F_r is the amplitude of the rth radial force wave. Throughout this paper, $B_r(r,kf)$ and $F_r(r,kf)$ denote radial flux-density and radial force harmonics, respectively. The first index r is the mechanical spatial order, defined as the number of spatial cycles around the full circumference; the second index specifies the temporal frequency kf, where k is the temporal harmonic order relative to the fundamental electrical frequency $f = pn/60$. Here, p is the number of pole pairs and n is the speed in rpm. For example, $B_r(52,13f)$ has mechanical spatial order 52 and temporal frequency $13f$. The same convention applies to tangential components. Torque is closely related to the tangential force. From the Maxwell stress tensor,

$$F_t(\theta,t) = \frac{1}{\mu_0}B_r(\theta,t)B_t(\theta,t) \tag{11}$$

Equations (5)–(11) show that armature MMF, permanent-magnet MMF, and permeance harmonics jointly determine the radial force-wave orders. A zeroth-order or low-order wave produces global radial deformation. Its response is amplified when its frequency approaches a structural natural frequency. The optimization should therefore reduce low-order radial forces at the critical frequencies.

2.3. Vibration Suppression Through Air-Gap-Domain Topology Optimization

The preceding derivation shows that MMF–permeance coupling determines the spatial orders and frequencies of radial force waves. The key waves can therefore be changed by adjusting local air-gap permeance without significantly reducing average torque. This study applies topology optimization to reconstruct the local air-gap geometry and reduce vibration at its source. The candidate design region includes the stator slot openings, the effective air-gap boundary, and the near-surface rotor region. A variable component $\Delta\Lambda(\theta,t)$ is added to the original permeance $\Lambda(\theta,t)$. It redirects local flux paths and changes the radial force-wave amplitudes. The objective directly targets low-order radial forces and their vibration response. This differs from methods that only correct isolated flux-density harmonics. A normalized Gaussian network (NGnet) provides high design freedom and smooth, manufacturable boundaries. Figure 2 illustrates the Gaussian basis functions, their weighted combination, and threshold-based material assignment. Continuous two-dimensional Gaussian basis functions describe the material distribution. A threshold then converts each continuous variable into air or iron. Compared with a conventional ON/OFF

method, NGnet reduces isolated cells and jagged edges. The basis functions and material rule are

$$G_i(x,y) = \frac{1}{2\pi s_G^2} \exp\left[-\frac{\|x-x_i\|^2 + \|y-y_i\|^2}{2s_G^2}\right] \tag{12}$$

$$b_i(x,y) = \frac{G_i(x,y)}{\sum_{i=0}^{N-1} G_i(x,y)} \tag{13}$$

$$M_n(x,y) = \sum_{i=0}^{21} \omega_i b_i(x,y) \tag{14}$$

$$A_n(x,y) = \begin{cases} \text{air}, & M_n(x,y) \le \eta, \\ \text{iron}, & M_n(x,y) > \eta. \end{cases} \tag{15}$$

where (x_i, y_i) is the center of the ith Gaussian function, s_G is its scale parameter, ω_i is its weight, and η is the material-assignment threshold. Changing ω_i continuously evolves the local air-gap topology.

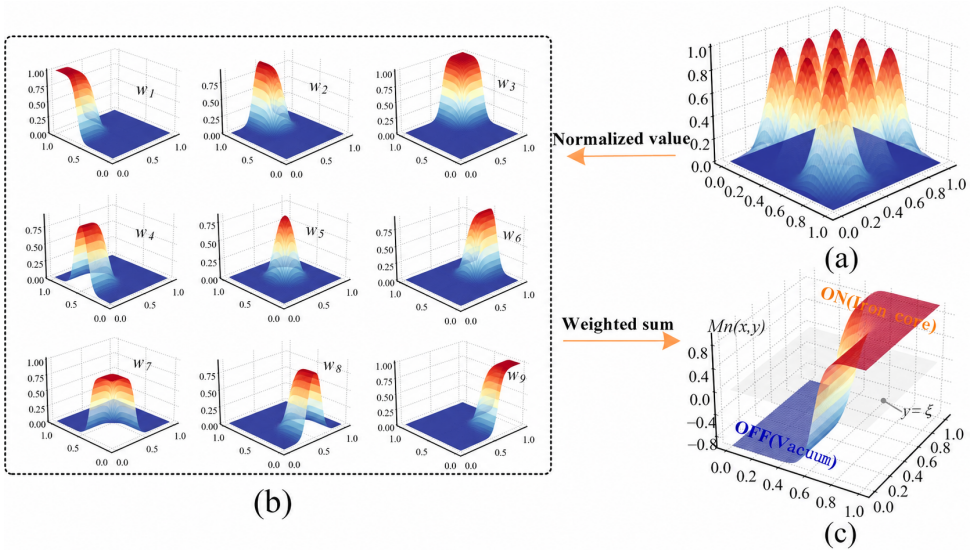


Figure 2. Principle of NGnet-based topology optimization: (**a**) normalized Gaussian basis functions; (**b**) weighted combination of the Gaussian basis functions; and (**c**) threshold-based material assignment.

The NGnet-based procedure is summarized below. N continuous Gaussian functions $G_i(x,y)$ are placed in the prescribed design domain, which is divided into n microcells. Equation (12) defines the Gaussian basis functions $G_i(x,y)$. Equation (13) computes the normalized basis functions $b_i(x,y)$, whose sum at each location equals unity. Equation (14) computes the weighted material parameter $M_n(x,y)$ for each cell. Each cell receives a binary material label $A_n(x,y)$: 0 for air and 1 for iron. Equation (15) compares $M_n(x,y)$ with the threshold η to assign the material. Cells with the same material are merged to form a new topology. A finite-element model then evaluates radial force waves and vibration at each operating condition. Low-order radial force, torque performance, structural safety, and manufacturability are used as objectives or constraints. This process suppresses electromagnetic excitation while retaining the main electromagnetic performance.

3. Multi-Operating-Condition Air-Gap-Domain Optimization

3.1. Design Example

To verify the effectiveness of the proposed air-gap-domain topology optimization method, a permanent-magnet traction motor with a six-layer hairpin winding is selected as the design case. The motor adopts a combined $\Delta + U$-shaped rotor topology and is representative of high-power-density electric-drive applications. Figure 3 shows an exploded view of the design-case motor, including the rotor, stator, hairpin winding, cooling-oil channel, housing, and front and rear covers. The rectangular conductors provide a high slot fill factor and favorable heat dissipation, whereas the compact electromagnetic and structural arrangement makes the motor susceptible to electromagnetic vibration and noise under wide-ranging operating conditions. The main motor parameters and specified performance targets are summarized in Table 1.

Table 1. Main motor parameters and specified performance targets.

Parameter	Value
Rated power (kW)	40
Rated torque (N·m)	>70
Peak power (kW)	>100
Peak torque (N·m)	>160
Rated speed (rpm)	6000
Maximum design speed (rpm)	16,000
DC-link voltage (V)	630
Number of stator slots	48
Number of rotor poles	8
Air-gap length (mm)	1.2
Permanent-magnet grade	N52UH
Core material	Silicon steel
Core-material yield strength (MPa)	Approximately 430
Winding type	6-layer hairpin winding

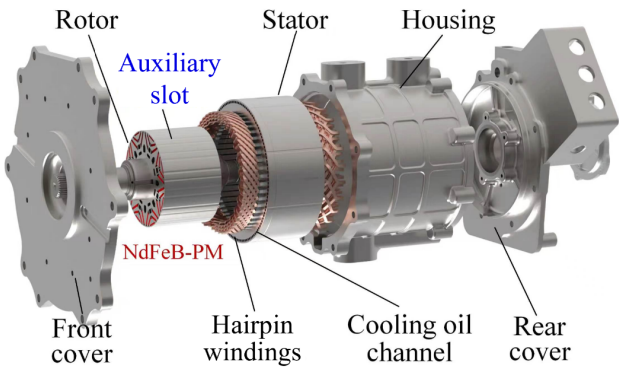


Figure 3. Three-dimensional structure of the design-case motor.

Figure 4 presents the equivalent radiated power (ERP) waterfall map of the design-case motor over the speed range. The stator breathing mode lies within the 6–8 kHz band, with the highlighted response occurring near 6.77 kHz. The dominant excitation associated with this resonance is the radial electromagnetic force harmonic at $12f$. As motor speed increases, the frequency of this force harmonic rises and approaches the breathing-mode natural frequency, amplifying the structural vibration and radiated noise. This resonance mechanism motivates the suppression of the $12f$ radial electromagnetic force harmonic in the subsequent air-gap-domain topology optimization.

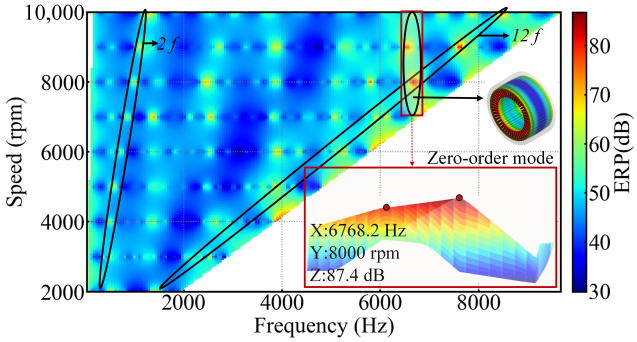


Figure 4. Equivalent radiated power (ERP) waterfall map of the design-case motor.

3.2. Characteristic Electromagnetic Forces

To further analyze the electromagnetic excitation of the motor, finite-element analysis (FEA) is used to calculate the air-gap force distributions over space and time under no-load and loaded conditions. A two-dimensional fast Fourier transform (2D FFT) is then applied to identify the spatial and temporal force harmonics. Figure 5 shows the air-gap force waveform and its spatiotemporal harmonics over one pole pair at rated load. Armature MMF couples with permanent-magnet MMF and permeance harmonics, so loading increases both the force amplitude and the number of harmonics. The strongest terms are the zeroth-order tooth-frequency components $(0, (Z/2p)f)$ and $(0, (Z/p)f)$. The lowest nonzero spatial order is eight. Because structural response decreases rapidly with spatial order, the subsequent analysis focuses on zeroth-order and tooth-order components. Figure 5c shows the tangential force waveform at rated load. Its spatial distribution resembles the radial force but its amplitude is lower. The positive $(0, 0f)$ tangential component confirms torque production. Radial force is therefore the primary NVH excitation, while tangential force is retained because it affects torque ripple and coupled vibration.

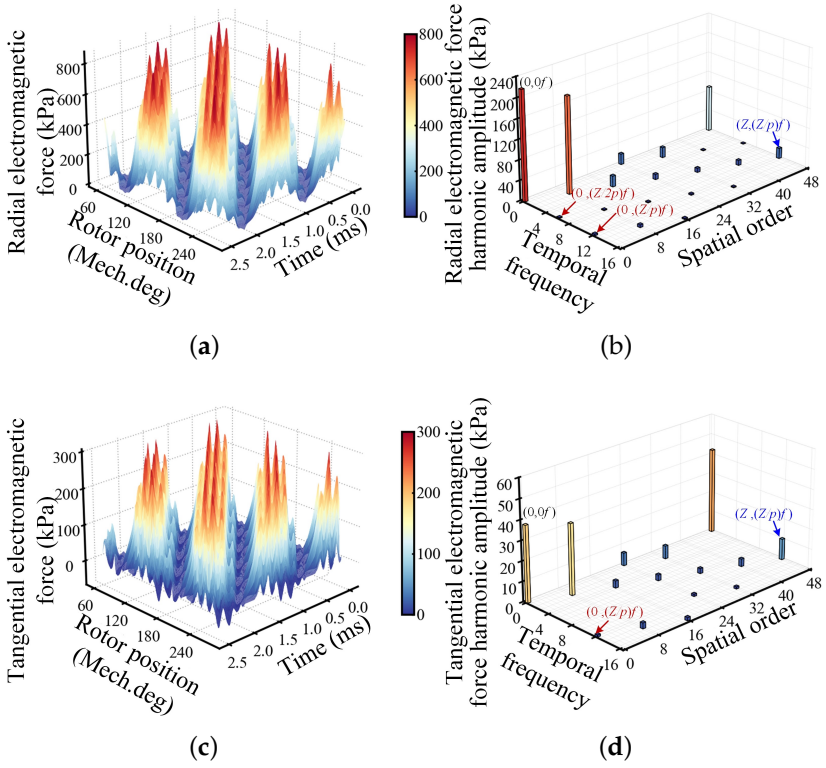


Figure 5. Radial and tangential force waveforms and spatiotemporal harmonics of the baseline motor at rated load: (**a**) loaded radial force waveform; (**b**) radial spatiotemporal harmonics; (**c**) loaded tangential force waveform; and (**d**) tangential spatiotemporal harmonics.

The dominant excitations are low-order and tooth-frequency force waves. For the combined $\Delta + U$-shaped rotor, MMF–permeance coupling strongly affects $F_r(0, 6f)$, $F_r(0, 12f)$, and $F_r(48, 12f)$. $F_t(0, 12f)$ is closely related to torque ripple. The topology optimization therefore targets these force components while constraining average torque, torque ripple, and manufacturability.

3.3. Effects of d- and q-Axis Currents on Characteristic Forces

Changes in armature current alter the armature MMF, distort the air-gap field, and change the amplitude and phase of characteristic force harmonics. Uniform sampling of i_d and i_q combined with FEA is used to map the key harmonics over the full operating range. Figure 6 shows the results.

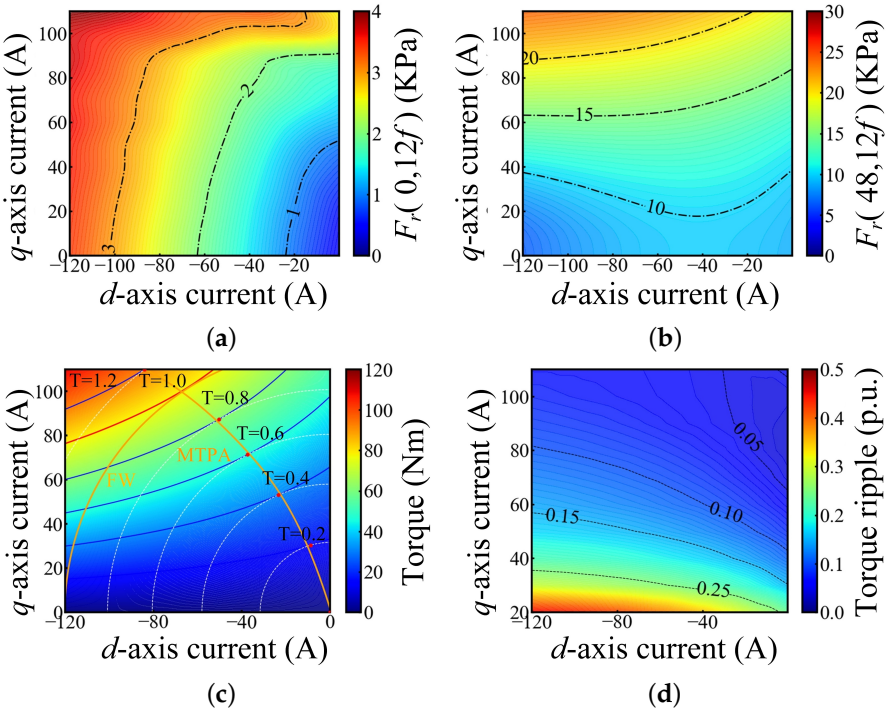


Figure 6. Variation of key radial force harmonics and torque performance with d- and q-axis currents: (**a**) $F_r(0, 12f)$; (**b**) $F_r(48, 12f)$; (**c**) average torque; and (**d**) torque ripple.

Figure 6c,d show average torque and torque ripple, respectively, as functions of i_d and i_q. Torque increases with current magnitude. The motor uses maximum-torque-per-ampere (MTPA) control in the low-speed region, flux-weakening (FW) control at medium-to-high speed, and maximum-torque-per-voltage (MTPV) control near the voltage limit. Torque ripple decreases along the low-speed control trajectory but becomes positively correlated with i_d in the flux-weakening region. High-speed torque ripple therefore requires explicit suppression. Figure 6a,b show the characteristic radial force harmonics $F_r(0, 12f)$ and $F_r(48, 12f)$, respectively. $F_r(0, 12f)$ generally rises with current and remains large in both low-speed high-load and high-speed light-load regions. $F_r(48, 12f)$ follows the torque trend and is mainly governed by i_q. The selected optimization terms are $F_r(0, 12f)$ and $F_r(48, 12f)$ at the low-speed high-load point OC1, and $F_t(0, 12f)$ and $F_r(0, 12f)$ at the high-speed light-load point OC2. Their dominant flux-density harmonics are then identified for targeted optimization. The force amplitudes are projected onto the speed–torque plane. K-means clustering selects two representative operating points, listed in Table 2. Hereafter, the low-speed high-load condition (OC1) and high-speed light-load condition (OC2) are used as the representative operating points. These points cover both operating regions, so the optimized structure is not tied to one operating point.

Table 2. Selected representative operating conditions.

Condition	i_d (A)	i_q (A)	n (rpm)	Angle (deg)
OC1	−53	99	3000	28.16
OC2	−95	46	12,000	64.16

3.4. Multi-Objective Optimization Model

Figure 7 shows the air-gap design domain and Gaussian-cell grid. The domain includes the initial air gap, the rotor-edge region, and the stator-tooth-edge region. It is divided into 3000 microcells. Twenty-two Gaussian functions $G_i(x, y)$ are placed at one-third and two-thirds of the radial span. Their normalized weighted sum defines $M_n(x, y)$, and the threshold rule defines $A_n(x, y)$. To reduce prototype cost and ensure manufacturability, only the rotor-edge contour is modified. Stator-edge cells remain iron, while the slot-opening and initial-gap cells remain air. After identifying the key force components at OC1 and OC2, the 22 Gaussian weights $\omega_0, \omega_1, \ldots, \omega_{21}$ are used as design variables. Each weight vector generates a rotor-edge geometry. FEA evaluates its average torque, torque ripple, structural stress, and characteristic force amplitudes.

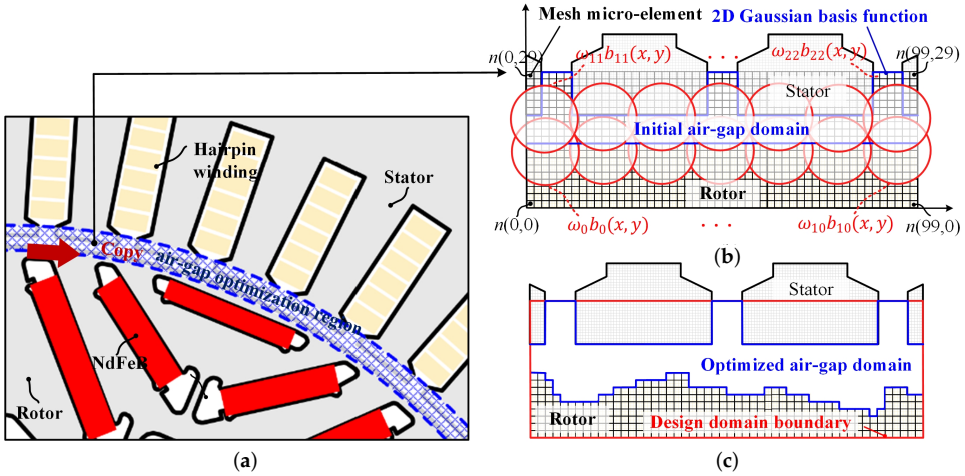


Figure 7. Air-gap design domain and Gaussian-cell discretization: (**a**) air-gap optimization region in the motor cross-section; (**b**) initial air-gap domain with the micro-element mesh and two-dimensional Gaussian basis functions; and (**c**) optimized air-gap design domain and its boundary.

Changes in the air-gap geometry directly modify the air-gap flux-density harmonics. According to the Maxwell stress expressions in Equations (8) and (11), the characteristic force harmonics arise from interactions between flux-density harmonics. Their amplitudes therefore depend on both the magnitudes and relative phases of the contributing harmonics. To connect the air-gap topology to the optimization targets, the dominant contributions to $F_r(0, 12f)$, $F_r(48, 12f)$, and $F_t(0, 12f)$ are examined using vector synthesis.

Figure 8 shows that interactions involving $B_r(52, 13f)$ and $B_r(44, 11f)$ provide major contributions to $F_r(0, 12f)$ at both operating points. The dominant contribution to $F_r(48, 12f)$ at OC1 involves $B_r(52, 13f)$, whereas $B_r(44, 11f)$ provides an important contribution to $F_t(0, 12f)$ at OC2 through its interaction with a tangential flux-density harmonic. These vector relationships indicate that force reduction requires coordinated adjustment of the contributing harmonics rather than a uniform reduction in all harmonic amplitudes. In particular, reducing $B_r(52, 13f)$ and strengthening the opposing contribution associated with $B_r(44, 11f)$ at OC2 provide a basis for suppressing the resultant characteristic forces. Air-gap-domain topology optimization therefore targets these key flux-density

harmonics to reduce electromagnetic excitation at both operating points and improve vibration performance.

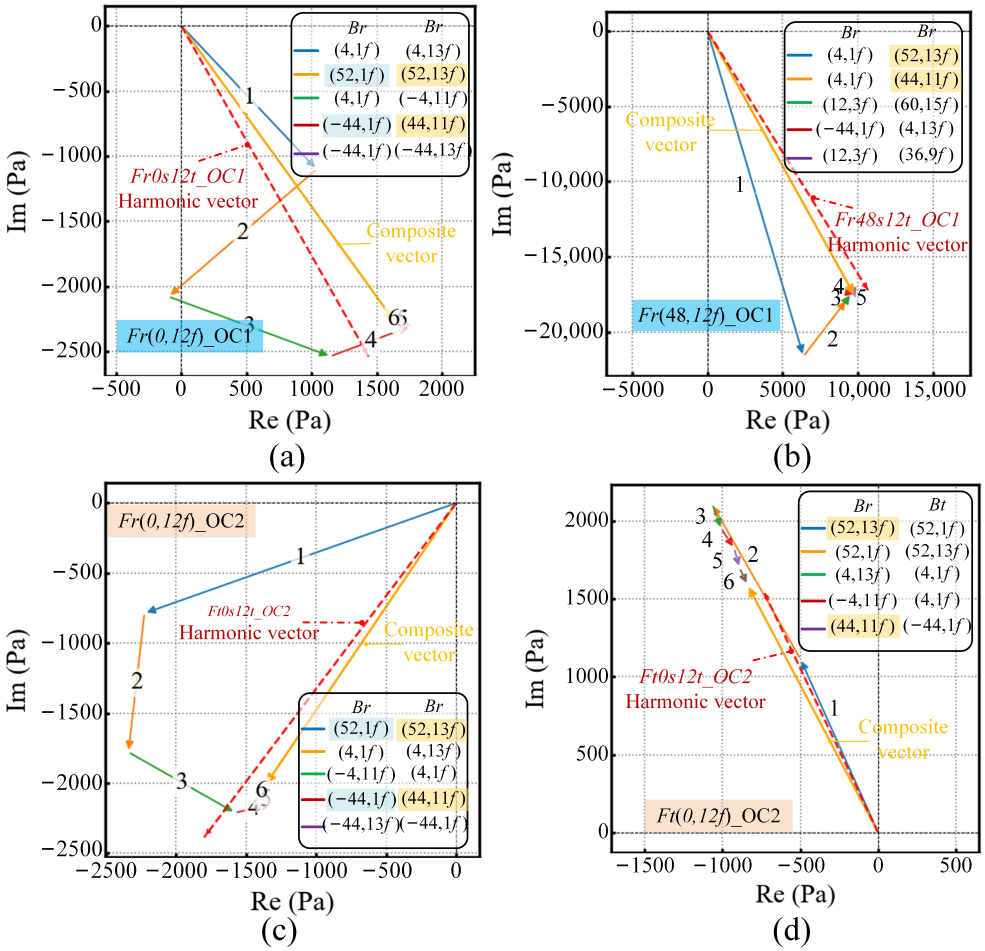


Figure 8. Vector synthesis of characteristic electromagnetic force harmonics under OC1 and OC2: (**a**) $F_r(0, 12f)$ at OC1; (**b**) $F_r(48, 12f)$ at OC1; (**c**) $F_r(0, 12f)$ at OC2; and (**d**) $F_t(0, 12f)$ at OC2.

Based on the above analysis, this study proposes a multi-objective flux-density optimization model based on topology optimization, targeting the harmonics $B_r(52, 13f)$ and $B_r(44, 11f)$ while constraining average torque and rotor-edge stress. These constraints ensure that vibration reduction does not compromise electromagnetic performance or structural safety.

$$\begin{aligned} \min_{\mathbf{X}} \quad & f_1(\mathbf{X}) = B_r(52, 13f)_{\mathrm{OC1}}(\mathbf{X}), \\ \max_{\mathbf{X}} \quad & f_2(\mathbf{X}) = B_r(44, 11f)_{\mathrm{OC2}}(\mathbf{X}), \\ & \mathbf{X} = [\omega_0, \omega_1, \ldots, \omega_{21}]^{\mathrm{T}}, \\ \text{subject to} \quad & 0 \le \omega_i \le 1, \quad i = 0, 1, \ldots, 21, \\ & g_1(\mathbf{X}) = \frac{B_r(4, 1f)(\mathbf{X})}{B_r(4, 1f)_{\mathrm{initial}}} \in [1, 1.05], \\ & g_2(\mathbf{X}) = \frac{\sigma_{\max}(\mathbf{X})}{\sigma_{\max}^{\mathrm{initial}}} \in [1, 1.20]. \end{aligned} \tag{16}$$

The two objectives are optimized simultaneously using NSGA-II. The first objective minimizes the amplitude of $B_r(52, 13f)$ at OC1, while the second objective maximizes the amplitude of $B_r(44, 11f)$ at OC2. The design vector $\mathbf{X} = [\omega_0, \omega_1, \ldots, \omega_{21}]^{\mathrm{T}}$ contains

the 22 Gaussian weights and is used consistently in all objective and constraint functions. Non-dominated sorting identifies Pareto-optimal tradeoffs between the two objectives. The fundamental air-gap harmonic $B_r(4, 1f)$ contributes strongly to average torque, so constraint g_1 limits its change. Topology reconstruction can also create thin magnetic bridges at the rotor edge. Constraint g_2 limits the increase in maximum rotor stress to 20% relative to the baseline at the same rotational speed.

3.5. Optimization Process and Final Topology

NSGA-II is employed to solve the optimization model formulated in Equation (16). The algorithm parameters are listed in Table 3. During the optimization process, NSGA-II updates the 22 Gaussian weights through selection, crossover, and mutation. NGnet maps each weight vector to $A_n(x, y)$ and generates a rotor-edge topology. FEA then computes average torque, torque ripple, structural stress, and key force components. Non-dominated sorting and crowding distance retain the best tradeoff solutions. Figure 9 shows the iteration histories of the objectives and torque at both operating points. The target harmonic $B_r(52, 13f)$ at OC1 decreases from 0.07 T to about 0.03 T after 20 generations, a reduction of more than 57%. At OC2, it converges from 0.07 T to about 0.05 T. The beneficial harmonic $B_r(44, 11f)$ at OC2 increases from 0.01 T to about 0.02 T after 30 generations. These trends indicate stable convergence.

Table 3. NSGA-II algorithm settings.

Parameter	Value or Definition
Population size	200
Number of generations	50
Crossover probability	0.9
Mutation probability	1/22
Stopping criterion	Maximum of 50 generations
Number of independent runs	3 runs with different random seeds

Figure 9d shows that torque fluctuates and initially decreases as the force objectives improve. The constraint on $B_r(4, 1f)$ then restores and stabilizes torque. The multi-objective formulation therefore reduces characteristic excitation while maintaining the basic torque performance.

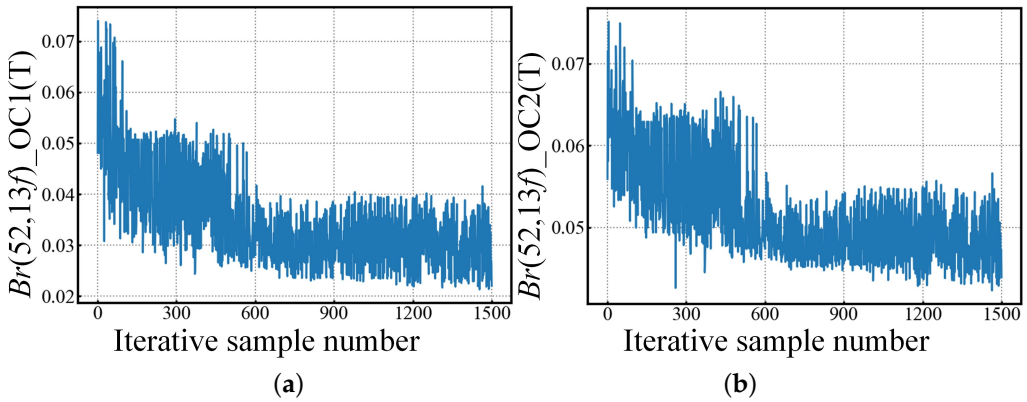


Figure 9. *Cont.*

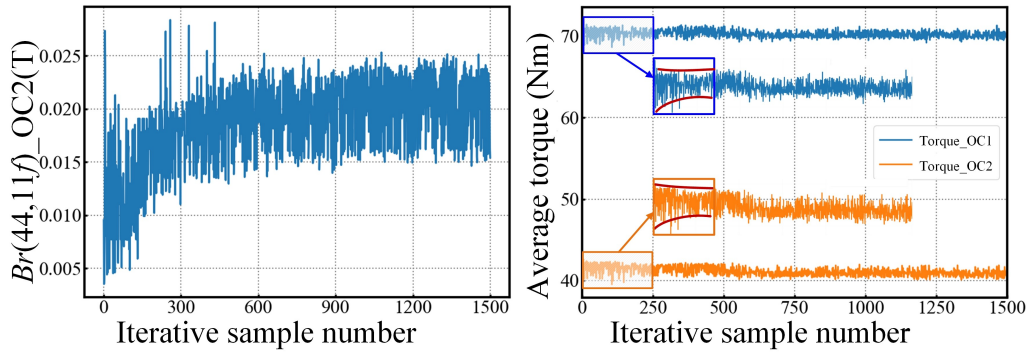


Figure 9. Iteration histories of the optimization objectives and torque: (**a**) $B_r(52, 13f)$ at OC1; (**b**) $B_r(52, 13f)$ at OC2; (**c**) $B_r(44, 11f)$ at OC2; and (**d**) average torque at OC1 and OC2.

Figure 10 shows the topology evolution. During the first 20 generations, the stator and rotor boundaries change frequently and form a continuous but irregular air gap. The large air region temporarily disturbs the main flux path and reduces torque. Later, the torque constraint shrinks the air region and stabilizes the topology. Two irregular, approximately elliptical slots finally form near the rotor edge. They avoid the main flux path while adjusting local permeance and reducing key force waves.

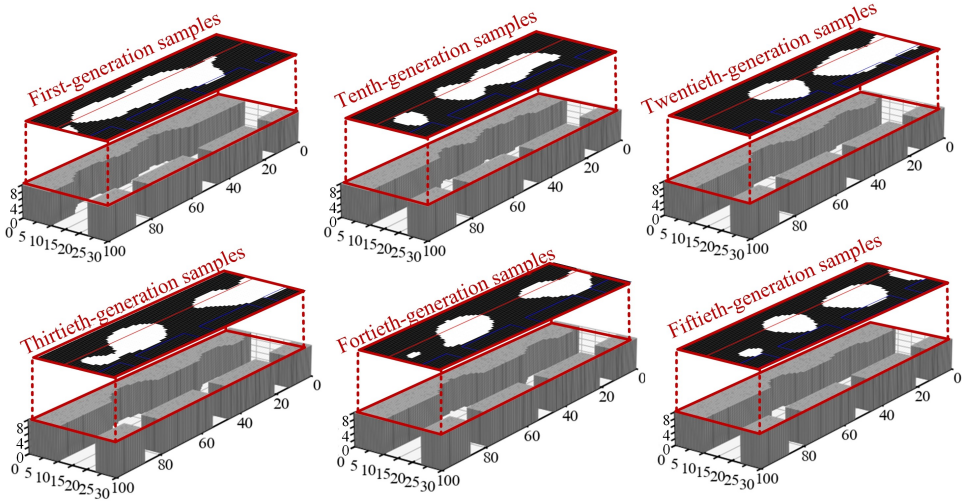


Figure 10. Evolution and convergence of the air-gap topology.

Figure 11 shows the final objective-space samples and Pareto front. The clear non-dominated set confirms a tradeoff between electromagnetic performance and vibration suppression. Minimizing $B_r(52, 13f)$ at OC1 and maximizing $B_r(44, 11f)$ at OC2 are competing objectives, so improving one may come at the expense of the other. NSGA-II preserves diverse tradeoff solutions through elitist selection and crowding distance, allowing for multiple mutually non-dominated solutions to remain in the final population. Several representative solutions have similar auxiliary-slot shapes, which indicates convergence to a stable feature. The Pareto solutions are screened using the following torque and stress limits, together with the manufacturability requirements:

$$\begin{cases} T_{\mathrm{avg},k}(\mathbf{X}) \geq 0.95\, T_{\mathrm{avg},k}^{\mathrm{initial}}, & k \in \{\mathrm{OC1}, \mathrm{OC2}\}, \\ r_{T,k}(\mathbf{X}) \leq 1.50\, r_{T,k}^{\mathrm{initial}}, & k \in \{\mathrm{OC1}, \mathrm{OC2}\}, \\ \sigma_{\max}(\mathbf{X}) \leq 430\ \mathrm{MPa}. \end{cases} \tag{17}$$

where $T_{\mathrm{avg},k}$ and $r_{T,k}$ denote average torque and torque ripple at operating point k, respectively, and $\sigma_{\max}$ is the maximum rotor stress over the evaluated speed range. Sample 1466 is selected as a compromise between the two optimization objectives. The selected topology is smoothed to remove jagged edges and support lamination stamping, as shown in Figure 12.

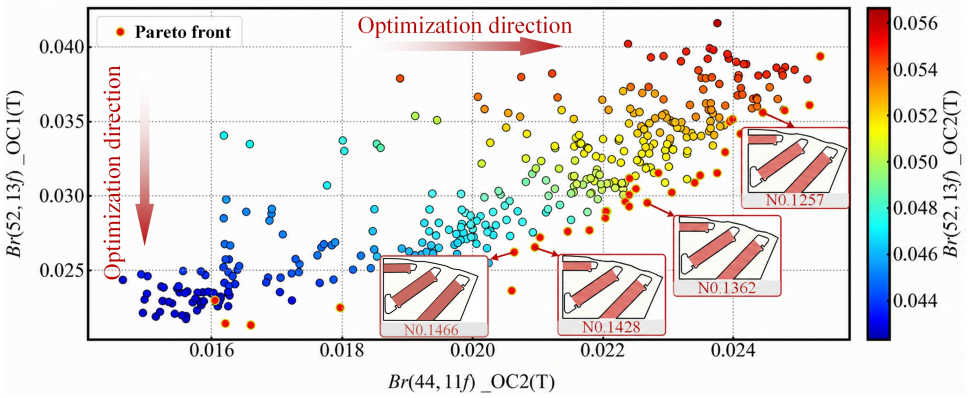


Figure 11. Optimization results and Pareto front.

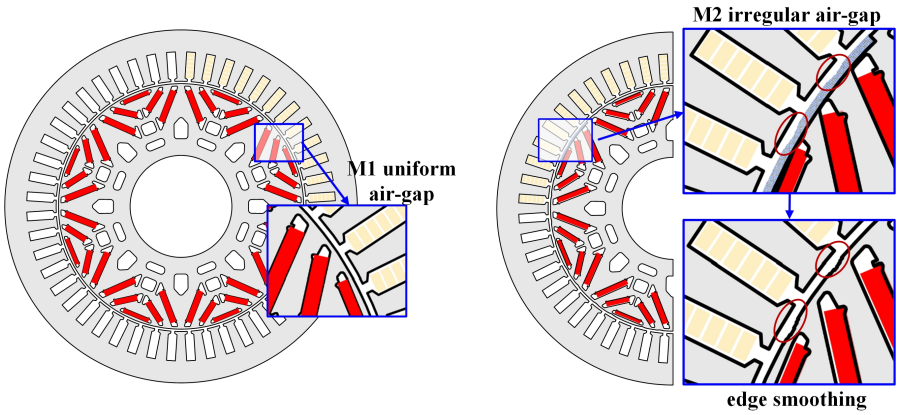


Figure 12. Air-gap-domain geometries before and after optimization: (**a**) baseline geometry; and (**b**) optimized geometry.

The rotor contour is extracted from the microcell boundary centerline, and local sharp corners are rounded. The smoothed contour maintains tangent continuity at joined segments and contains no sharp corners or isolated material islands. The final rotor contains only two local auxiliary slots near the air gap, arranged symmetrically about the magnetic pole axis. This limited change reduces the targeted electromagnetic excitations while retaining the main rotor topology. The two slots lie mainly ahead of the edge flux barriers and avoid the main flux paths. They reduce characteristic air-gap harmonics under different loads while maintaining torque. Their effects on torque ripple and vibration are evaluated at OC1 and OC2 in Section 4. Table 4 lists preliminary geometric limits and stamping requirements for the smoothed rotor contour.

Table 4. Manufacturability criteria for the smoothed rotor contour.

Criterion	Required Limit or Verification
Minimum magnetic-bridge thickness	≥1.0 mm
Minimum auxiliary-slot width	≥0.8 mm
Minimum auxiliary-slot length	≥2.0 mm
Minimum corner radius	≥0.5 mm
Lamination thickness	0.27 mm

4. Multiphysics Finite-Element Validation

4.1. Magnetic Flux-Density Distribution

A coupled Maxwell–Workbench model evaluates electromagnetic vibration and noise under multiple operating conditions. Modal superposition is used to compare the baseline motor (M1) and optimized motor (M2). For the Maxwell model, the mesh size, time step, boundary conditions, and convergence criteria are listed in Table 5.

Figure 13 compares the geometries and rated-condition flux-density contours of M1 and M2. The uniform air gap of M1 is locally modified by two auxiliary slots arranged symmetrically about the magnetic pole axis.

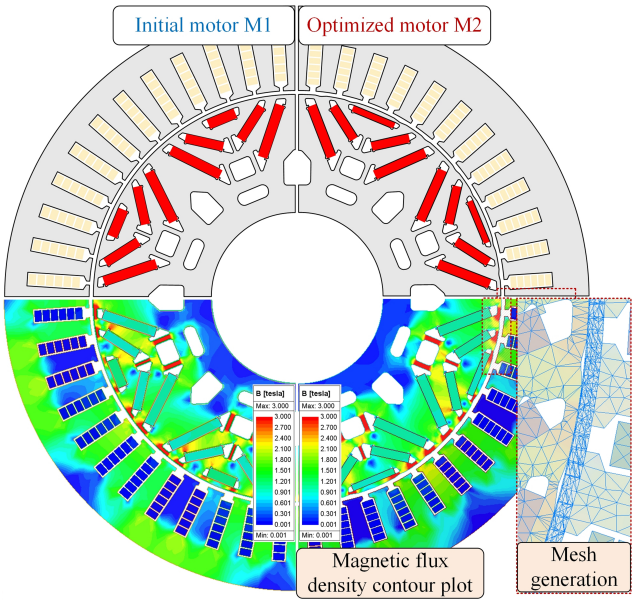


Figure 13. Motor geometries and magnetic flux-density contours for M1 and M2.

The flux density of M2 remains within a reasonable engineering range, and no severe local saturation appears. The two slots are located ahead of the edge flux barriers. They adjust local permeance while avoiding the main flux path. M2 therefore retains torque capability and provides a structural basis for reducing the key force waves.

Table 5. Setup parameters for the Maxwell electrical finite-element model.

Item	Setting
Air-gap mesh size	0.15 mm
Rotor/stator mesh size	1.0–2.0 mm
Slot edges' and magnetic bridges' mesh size	0.10 mm
Time step	$T_e/100$ (electrical period/100)
Magnetic boundary	Balloon boundary
Rotor motion	Rotating band
Convergence targets	Relative residual $\leq 10^{-6}$; period-to-period changes in torque and target forces $< 1\%$

4.2. Torque Performance

Figure 14 compares the torque of M1 and M2 at OC1 and OC2. At OC1, average torque decreases slightly from 70.9 to 70.4 N·m, while torque ripple increases from 5.9% to 7.5%. At OC2, average torque increases from 42.2 to 43.4 N·m. Suppression of $F_t(0, 12f)$ also reduces the torque harmonic at $12f$, and torque ripple decreases from 17.9% to 15.3%.

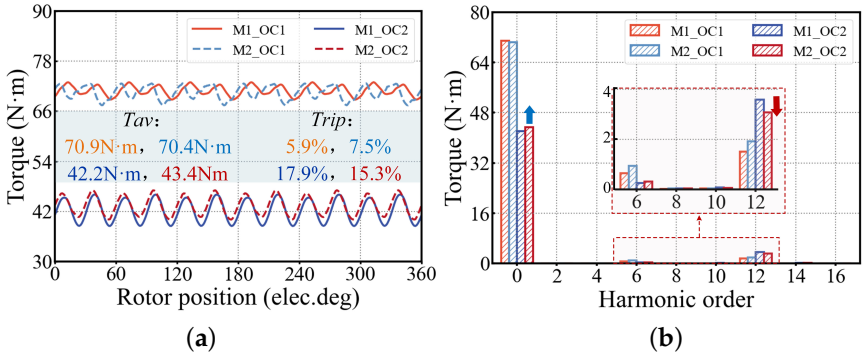


Figure 14. Torque performance for M1 and M2: (**a**) torque waveforms; and (**b**) torque harmonic spectra.

4.3. Air-Gap Flux Density Under Multiple Operating Conditions

Figure 15 compares the air-gap flux-density waveforms and Fourier spectra of M1 and M2. The harmonic order in these spectra denotes the temporal order k relative to the electrical fundamental frequency f. At OC1, the amplitude of $B_r(52, 13f)$ decreases from 0.044 to 0.031 T, a reduction of about 29.5%. The rotor topology of M2 therefore weakens a major source of the target radial force wave. At OC2, the amplitude of $B_r(52, 13f)$ decreases by about 11.4%, while that of $B_r(44, 11f)$ increases slightly. These changes reduce the key $F_r(0, 12f)$ and $F_t(0, 12f)$ excitations and show that the multi-objective strategy remains effective in different operating regions.

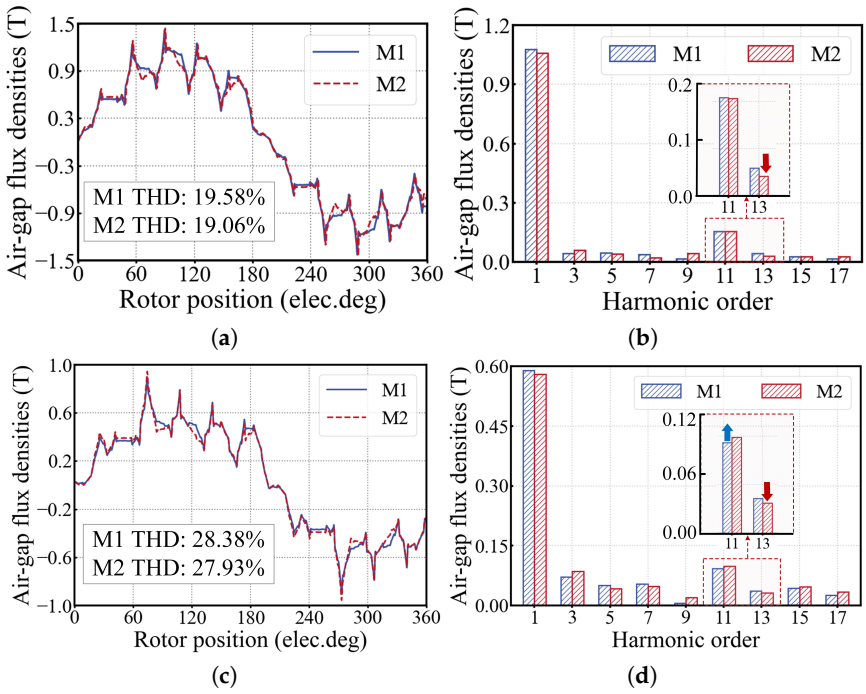


Figure 15. Air-gap flux density and harmonic spectra for M1 and M2: (**a**) air-gap flux-density waveform at OC1; (**b**) harmonic spectrum at OC1; (**c**) air-gap flux-density waveform at OC2; and (**d**) harmonic spectrum at OC2.

4.4. Characteristic Force Maps over the Full Speed Range

This section compares the full-speed-range distributions of the characteristic electromagnetic forces of M1 and M2.

Figure 16 compares $F_r(0, 12f)$ and $F_r(48, 12f)$. Suppression of the dominant $B_r(52, 13f)$ harmonic reduces $F_r(0, 12f)$ from 2.87 to 0.65 kPa at OC1 and from 2.99 to 1.76 kPa at OC2. Both reductions exceed 40%, and the full-speed-range map improves substantially. At OC1, $F_r(48, 12f)$ is also important. Its amplitude decreases from 20.27 to 8.61 kPa, a reduction of 57.52%. This result confirms effective suppression of the key radial force harmonics.

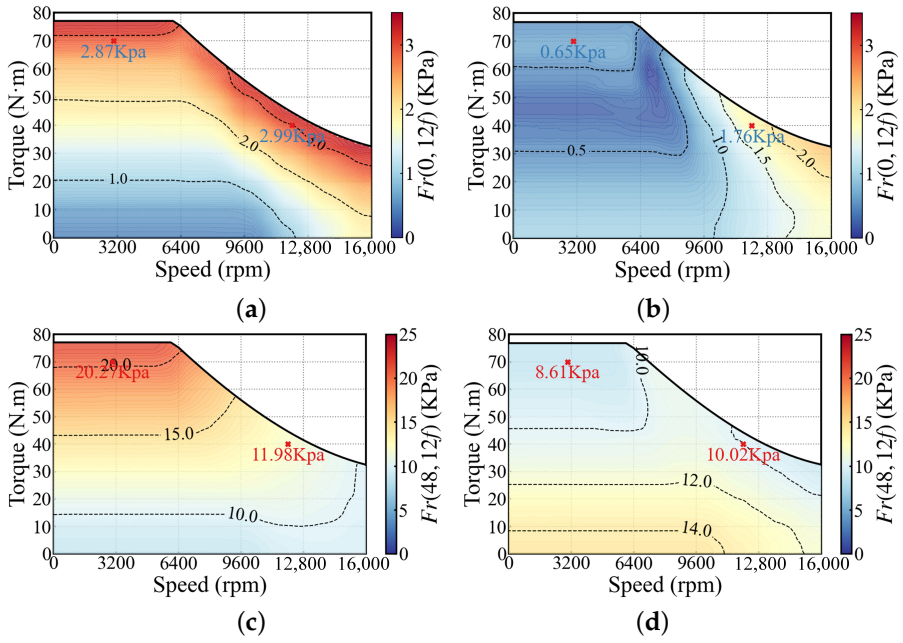


Figure 16. Full-speed-range maps of the characteristic radial electromagnetic forces for M1 and M2: (**a**) $F_r(0, 12f)$ for M1; (**b**) $F_r(0, 12f)$ for M2; (**c**) $F_r(48, 12f)$ for M1; and (**d**) $F_r(48, 12f)$ for M2.

4.5. Vibration Acceleration and Displacement

Subsequently, modal analysis and mode-superposition harmonic response analysis in Workbench are employed to investigate the motor vibration characteristics, using electromagnetic harmonic forces transferred from Maxwell as the excitation. The acceleration is evaluated at the top of the motor housing in the $+X$ direction, while displacement is reported as a spatial maximum over the structure.

Figure 17 compares the vibration acceleration spectra of M1 and M2 at OC1 and OC2. At OC1, a peak occurs at $12f$ (2400 Hz), as predicted by the mechanism analysis. Optimization reduces the acceleration from 2.19 to 0.30 m/s^2.

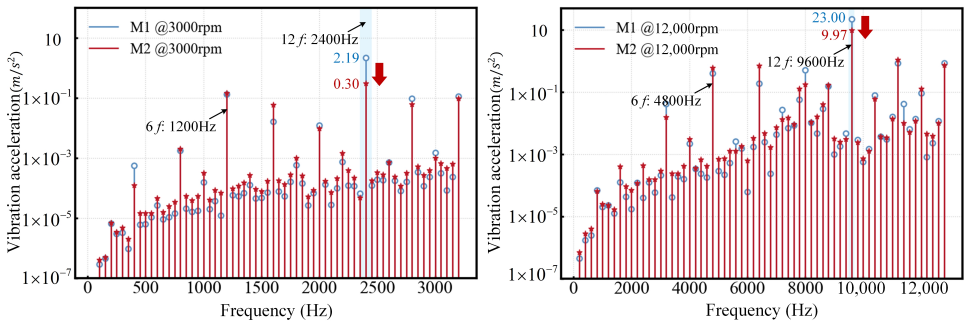


Figure 17. Vibration acceleration spectra at the representative operating conditions: (**a**) OC1; and (**b**) OC2.

At OC2, the $12f$ peak decreases from 23.00 to 9.97 m/s^2, a reduction of about 56.65%. The topology is therefore effective in both low-speed high-load and high-speed light-load operation. Figure 18 shows the displacement contours of M1 and M2. The maximum displacement at OC1 decreases from 1.14×10^{-4} to 6.60×10^{-5} mm, a reduction of about 42.1%. At OC2, it decreases from 4.23×10^{-4} to 3.38×10^{-4} mm.

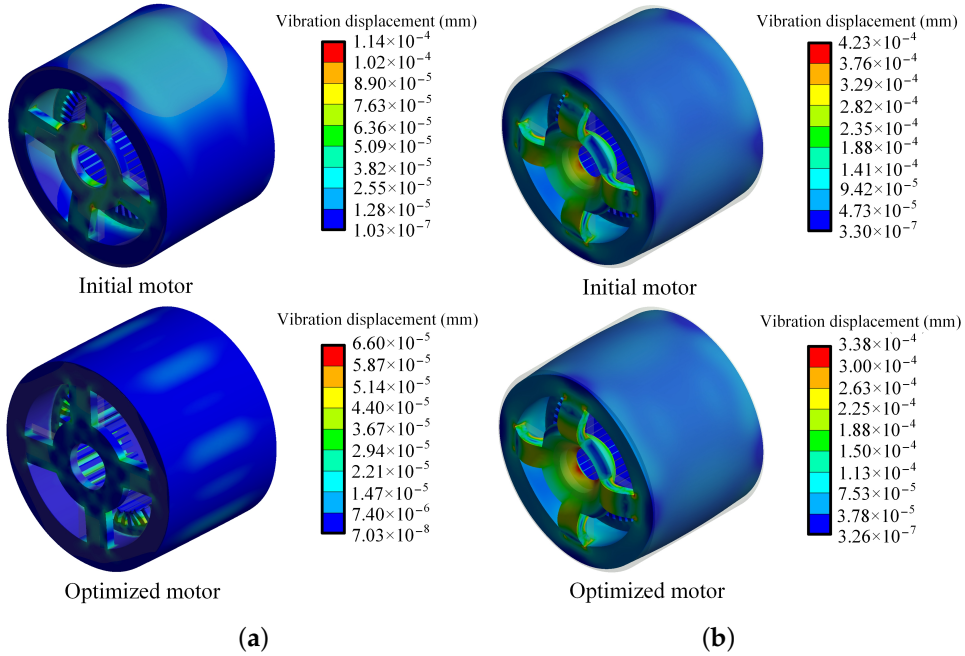


Figure 18. Structural displacement contours: (**a**) OC1; and (**b**) OC2.

4.6. Acoustic Performance

An acoustic finite-element and boundary-element model is used to compute sound-pressure contours and spectra. Table 6 lists the corresponding structural damping, modal boundary conditions, acoustic-domain settings, and mesh information. Figure 19 shows the sound-pressure-level contours on a cylindrical observation surface 0.5 m from the motor. The reported values are spatial maxima on this surface. The maximum SPL decreases from 44.27 to 43.23 dB at OC1 and from 68.95 to 67.20 dB at OC2, corresponding to reductions of 1.04 and 1.75 dB, respectively. SPL is based on RMS acoustic pressure. Acoustic radiation depends on the vibration distribution and phase over the radiating surface, so its reduction need not follow the local acceleration reduction.

Table 6. Setup parameters for the Workbench acoustic model.

Item	Setting
Structural damping	$\zeta_m = 0.02$
Modal boundary conditions	Supports at mounting and bearing locations; remaining exposed surfaces free
Structural mesh size	2.0 mm
Air properties	$\rho = 1.21$ kg/m^3; $c = 343$ m/s
Acoustic domain	Surrounding air with an exterior radiation condition
Acoustic mesh size	$\leq c/(10 f_{\max})$
Observation surface	0.5 m from the motor

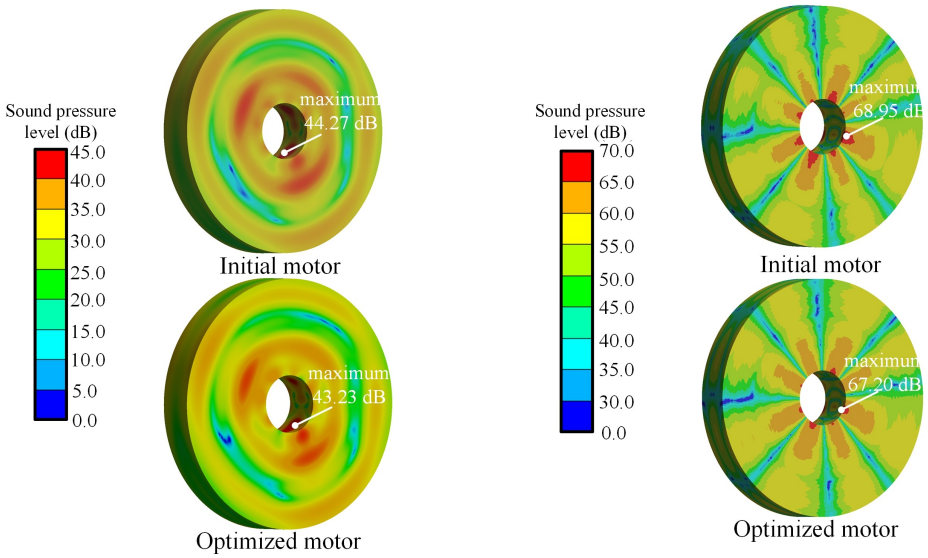


Figure 19. Radiated sound-pressure-level contours: (**a**) OC1; and (**b**) OC2.

Figure 20 compares the sound-pressure-level spectra for M1 and M2. At OC1, M2 has lower sound-pressure levels over most of the plotted frequency range. At OC2, the low-frequency levels are similar, while the level near 9600 Hz decreases after optimization.

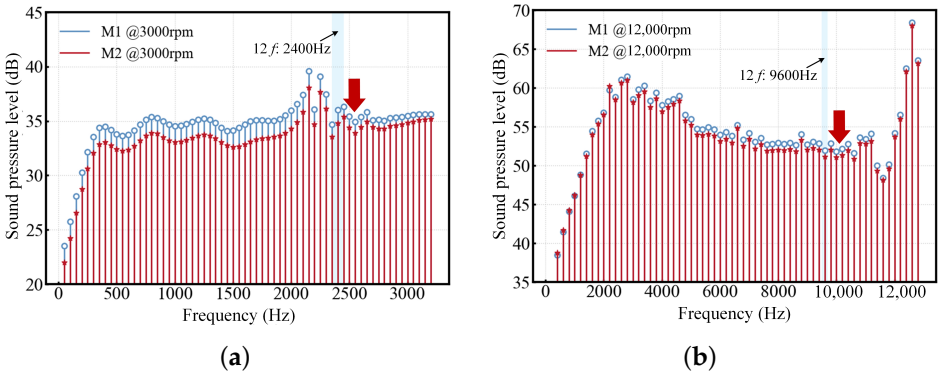


Figure 20. Sound-pressure-level spectra for M1 and M2: (**a**) OC1; and (**b**) OC2.

Figure 21 presents the rotor stress distributions under centrifugal loading. At 16,000 rpm, the maximum stress of M1 is 185.01 MPa and occurs near the reinforcing rib of the rectangular slot. In the rotor of M2, stress is concentrated near the magnetic bridges adjacent to the auxiliary slots. The maximum stresses are 51.22, 115.25, 204.90, and 320.15 MPa at 8000, 12,000, 16,000, and 20,000 rpm, respectively, increasing approximately with the square of rotational speed. At 16,000 rpm, optimization increases the maximum stress by 10.75%. At the highest evaluated speed of 20,000 rpm, the maximum stress remains below the specified yield strength of approximately 430 MPa, corresponding to a safety factor of 1.34. The rotor of M2 therefore satisfies the yield-strength requirement under the evaluated centrifugal loading conditions.

Finally, Table 7 summarizes the performance of M1 and M2 at OC1 and OC2. M2 reduces the characteristic radial force harmonics, vibration acceleration, displacement, and sound-pressure level (SPL) at both operating points while maintaining comparable average torque.

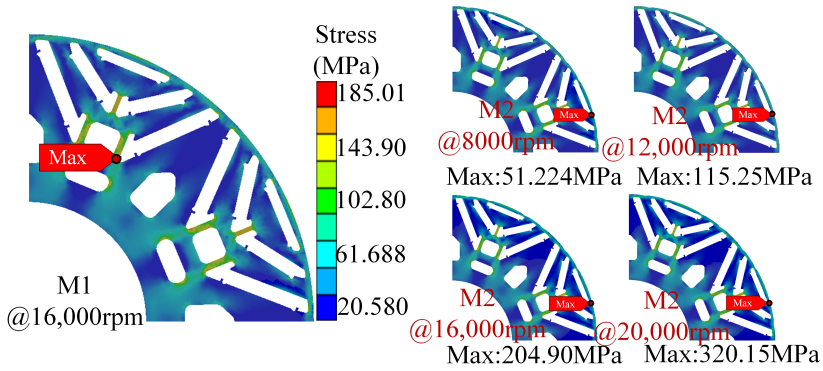


Figure 21. Rotor stress distributions under high-speed operation: M1 at 16,000 rpm and M2 with the smoothed rotor contour at 8000, 12,000, 16,000, and 20,000 rpm.

Table 7. Summary of simulation results for M1 and M2 at OC1 and OC2.

	OC1		OC2	
Quantity	**M1**	**M2**	**M1**	**M2**
Average torque (N·m)	70.9	70.4	42.2	43.4
Torque ripple (%)	5.9	7.5	17.9	15.3
$F_r(0, 12f)$ (kPa)	2.87	0.65	2.99	1.76
$F_r(48, 12f)$ (kPa)	20.27	8.61	11.98	10.02
$12f$ acceleration (m/s^2)	2.19	0.30	23.00	9.97
Maximum displacement (10^{-4} mm)	1.14	0.660	4.23	3.38
$12f$ SPL (dB)	44.27	43.23	68.95	67.20

5. Experimental Verification

5.1. Prototype Motor and Test Platform

To experimentally evaluate the proposed air-gap-domain topology optimization method, a 40 kW interior permanent-magnet motor incorporating the optimized rotor is manufactured. Test platforms are established to assess its electromagnetic performance and vibration and noise characteristics. Figure 22 shows the prototype motor, the electromagnetic and vibration/noise test setups, the rotor laminations, and the hairpin-wound stator.

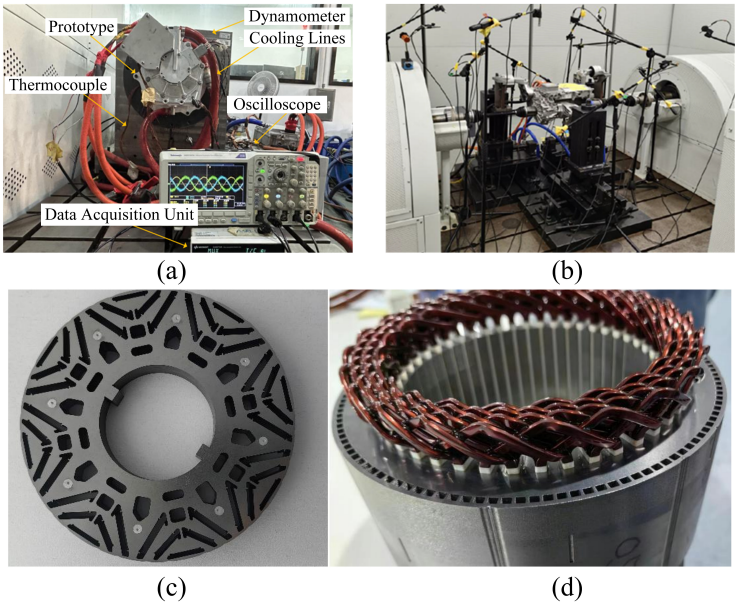


Figure 22. Prototype motor and experimental test platforms: (**a**) electromagnetic test setup; (**b**) vibration and noise test setup; (**c**) rotor laminations; and (**d**) hairpin-wound stator.

5.2. Electromagnetic Performance Test

The optimized prototype is first tested under no-load conditions at the rated speed of 6000 rpm. Figure 23 compares the measured and simulated back-EMF waveforms and their harmonic spectra obtained by Fourier decomposition. The measured fundamental amplitude is 421.78 V, compared with 449.23 V predicted by FEA, corresponding to a relative deviation of approximately 6.11% with respect to the simulated value. The measured total harmonic distortion (THD) is 5.21%, close to the simulated value of 5.26%. The differences may be associated with temperature-dependent magnet properties and manufacturing tolerances. The agreement in waveform shape and harmonic distortion supports the electromagnetic model of the optimized prototype.

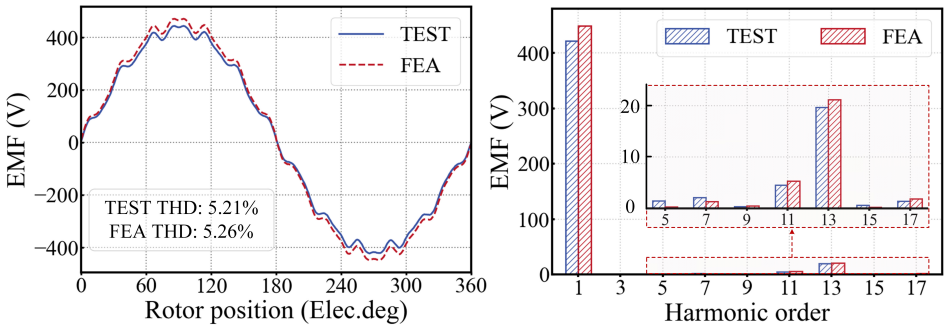


Figure 23. Measured and simulated no-load back-EMF of the optimized prototype at 6000 rpm: (**a**) waveforms; and (**b**) harmonic spectra.

5.3. Vibration and Noise Tests

The vibration and noise characteristics of the optimized prototype are subsequently measured. The accelerometer is mounted at the uppermost point on the motor housing (the $+X$ position), matching the simulation evaluation point, and measures acceleration in the $+X$ direction. The reported experimental acceleration amplitudes use the peak convention. Figure 24 presents the housing vibration acceleration spectra in the $+X$ direction at OC1 and OC2. The measured $12f$ acceleration amplitudes are 1.91 m/s^2 at OC1 and 7.98 m/s^2 at OC2. Additional high-frequency peaks are observed and may be associated with inverter carrier-related excitation. These components should be distinguished from the characteristic $12f$ excitation.

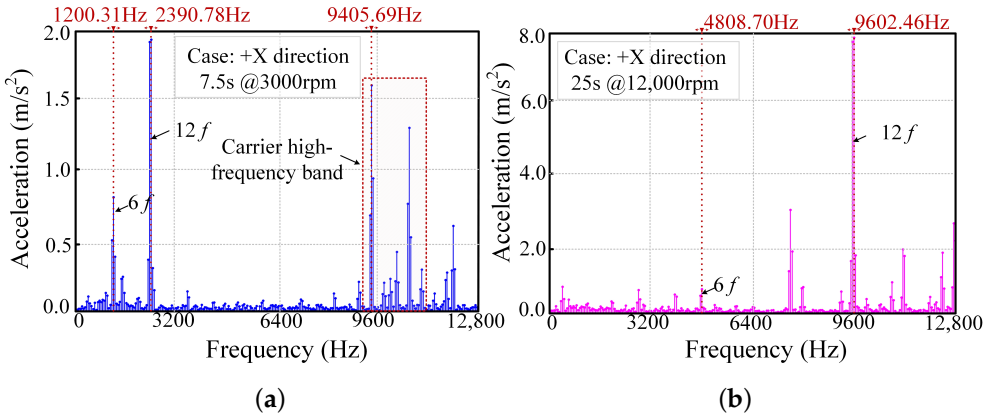


Figure 24. Measured housing vibration acceleration spectra of the optimized prototype in the $+X$ direction: (**a**) OC1 at 3000 rpm; and (**b**) OC2 at 12,000 rpm.

Figures 25 and 26 show the measured vibration acceleration and sound-pressure-level waterfall maps, respectively. Two speed sweeps are considered: 0–5000 rpm with a carrier

frequency of $f_c = 4$ kHz, and 0–16,000 rpm with $f_c = 10$ kHz. The $12f$ excitation trajectory is visible in both speed ranges, consistent with the predicted characteristic excitation frequency. Carrier-related bands are also observed, including the band near $2f_c = 8$ kHz in the low-speed sweep. At 3000 rpm, the reported $12f$ acceleration and sound-pressure level are 1.92 m/s^2 and 53.21 dB, respectively. At 12,000 rpm, the corresponding values from the speed-sweep tests are 12.05 m/s^2 and 71.40 dB. These measurements characterize the prototype response across the tested speed ranges; a quantitative experimental assessment of the improvement requires baseline measurements under matching conditions.

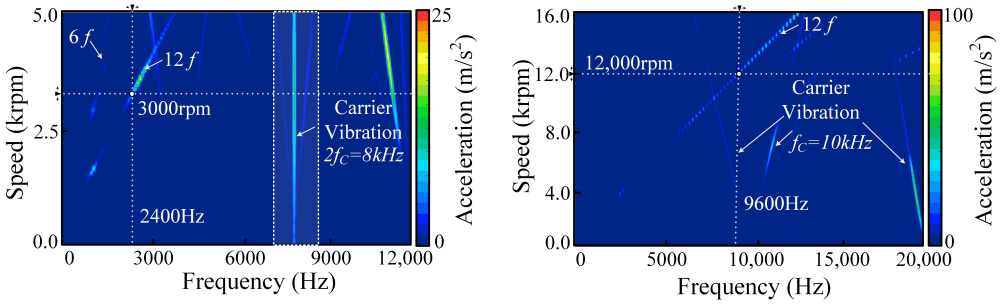


Figure 25. Measured vibration acceleration waterfall maps: (**a**) 0–5000 rpm with $f_c = 4$ kHz; and (**b**) 0–16,000 rpm with $f_c = 10$ kHz.

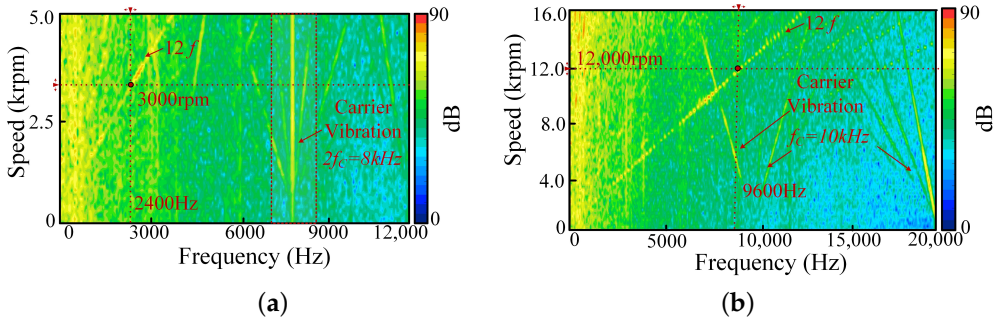


Figure 26. Measured sound-pressure-level waterfall maps: (**a**) 0–5000 rpm with $f_c = 4$ kHz; and (**b**) 0–16,000 rpm with $f_c = 10$ kHz.

6. Conclusions

This paper presents a harmonic-guided air-gap-domain topology optimization method for a 48-slot, eight-pole interior permanent-magnet motor with hairpin windings. The dominant flux-density contributions to the targeted force harmonics are identified by vector synthesis. A normalized Gaussian network represents the rotor-edge topology, and NSGA-II optimizes two flux-density objectives at low-speed high-load (OC1) and high-speed light-load (OC2) operating points subject to torque, stress, and manufacturability constraints. Multiphysics finite-element results indicate that $F_r(0, 12f)$ is reduced by more than 40% at both operating points and $F_r(48, 12f)$ by 57.52% at OC1. The $12f$ acceleration is reduced by 86.30% and 56.65% at OC1 and OC2, respectively. The maximum sound-pressure level on the evaluation surface is reduced by 1.04 and 1.75 dB, respectively, with comparable average torque. The peak rotor stress at 20,000 rpm is 320.15 MPa, below the specified yield strength of 430 MPa. Finally, a 40 kW optimized prototype is manufactured and tested for back-EMF, vibration, and noise. The measured back-EMF characteristics support the electromagnetic model, and the speed-sweep measurements identify the characteristic $12f$ response. The numerical and experimental results verify the effectiveness of the proposed method for electromagnetic vibration and noise reduction in traction motors.

Author Contributions: Conceptualization, J.W. and Z.X.; methodology, J.W. and Z.X.; software, J.W. and J.X.; validation, J.W., P.Z. and T.S.; formal analysis, J.W. and J.X.; investigation, J.W., P.Z. and T.S.; resources, J.W. and Z.X.; data curation, J.X., P.Z. and T.S.; writing—original draft preparation, J.W. and J.X.; writing—review and editing, J.W., J.X. and Z.X.; visualization, J.X.; supervision, Z.X.; project administration, Z.X.; funding acquisition, J.W. All authors have read and agreed to the published version of the manuscript.

Funding: This research was funded by the National Natural Science Foundation of China, grant number 52507059, and the Natural Science Foundation of Jiangsu Province, grant number BK20250871. The APC was funded by the National Natural Science Foundation of China.

Data Availability Statement: The raw data supporting the conclusions of this article will be made available by the authors on request.

Conflicts of Interest: Author Tengfei Song was employed by the company Suzhou Inovance Automotive Co., Ltd. The remaining authors declare that the research was conducted in the absence of any commercial or financial relationships that could be construed as a potential conflict of interest.

References

1. Chen, Z.; Liu, J. Exploring the Drive Motor of Electric Vehicles: Structure, Temperature Rises, and Operational Control of Permanent Magnet Motors. *World Electr. Veh. J.* **2024**, *15*, 483. https://doi.org/10.3390/wevj15110483.
2. Chen, H.; Demerdash, N.A.O.; El-Refaie, A.M.; Guo, Y.; Hua, W.; Lee, C.H.T. Investigation of a 3D-Magnetic Flux PMSM with High Torque Density for Electric Vehicles. *IEEE Trans. Energy Convers.* **2022**, *37*, 1442–1454. https://doi.org/10.1109/TEC.2021.3137803.
3. Xiang, Z.; Zhou, Y.; Zhu, X.; Liu, Q.; Quan, L. Research on Power Factor Enhancement of a Flux-Modulated PM Motor Utilizing a Slot-Space-Decoupled Stator Shifting Method. *IEEE Trans. Ind. Electron.* **2026**. https://doi.org/10.1109/TIE.2026.3732417.
4. Chen, H.; Tang, J.; Liu, Y.; Jiang, B.; Boscaglia, L. Electromagnetic Performance Investigation of a Brushless Electrically Excited Synchronous Machine for Long-Distance Heavy-Duty Electric Vehicles. *IEEE Trans. Transp. Electrif.* **2025**, *11*, 225–235. https://doi.org/10.1109/TTE.2024.3388430.
5. Ballo, F.; Gobbi, M.; Mastinu, G.; Palazzetti, R. Noise and Vibration of Permanent Magnet Synchronous Electric Motors: A Simplified Analytical Model. *IEEE Trans. Transp. Electrif.* **2023**, *9*, 2486–2496. https://doi.org/10.1109/TTE.2022.3209917.
6. Lu, Y.; Li, J.; Yang, K. A Hybrid Calculation Method of Electromagnetic Vibration for Electrical Machines Considering High-Frequency Current Harmonics. *IEEE Trans. Ind. Electron.* **2022**, *69*, 10385–10395. https://doi.org/10.1109/TIE.2022.3152021.
7. Gonzalez, P.; Buigues, G.; Mazon, A.J. Noise in Electric Motors: A Comprehensive Review. *Energies* **2023**, *16*, 5311. https://doi.org/10.3390/en16145311.
8. Han, Z.; Liu, J. Comparative Analysis of Vibration and Noise in IPMSM Considering the Effect of MTPA Control Algorithms for Electric Vehicles. *IEEE Trans. Power Electron.* **2021**, *36*, 6850–6862. https://doi.org/10.1109/TPEL.2020.3036402.
9. Xing, Z.; Zhao, W.; Wang, X.; Sun, Y. Reduction of Radial Electromagnetic Force Waves Based on PM Segmentation in SPMSMs. *IEEE Trans. Magn.* **2020**, *56*, 7507107. https://doi.org/10.1109/TMAG.2019.2952446.
10. Liang, W.; Wang, J.; Luk, P.C.K.; Fei, W. Analytical Study of Stator Tooth Modulation on Electromagnetic Radial Force in Permanent Magnet Synchronous Machines. *IEEE Trans. Ind. Electron.* **2021**, *68*, 11731–11739. https://doi.org/10.1109/TIE.2020.3029462.
11. Mao, Y.; Zhao, W.; Zhu, S.; Chen, Q.; Ji, J. Vibration Investigation of Spoke-Type PM Machine with Asymmetric Rotor Considering Modulation Effect of Stator Teeth. *IEEE Trans. Ind. Electron.* **2021**, *68*, 9092–9103. https://doi.org/10.1109/TIE.2020.3022530.
12. Xu, J.; Zhang, L.; Meng, D.; Su, H. Simulation, Verification and Optimization Design of Electromagnetic Vibration and Noise of Permanent Magnet Synchronous Motor for Vehicle. *Energies* **2022**, *15*, 5808. https://doi.org/10.3390/en15165808.
13. Zhou, X.; Zhu, X.; Xiang, Z.; Fan, D.; Xu, L.; Zhu, T. Harmonic-Oriented Design and Vibration Characteristic Suppression for Interior Permanent Magnet Motors. *IEEE Trans. Ind. Electron.* **2024**, *71*, 1246–1256. https://doi.org/10.1109/TIE.2023.3262863.
14. Xing, Z.; Wang, X.; Zhao, W. Optimization of Stator Slot Parameters for Electromagnetic Vibration Reduction of Permanent Magnet Synchronous Motors. *IEEE Trans. Transp. Electrif.* **2022**, *8*, 4337–4347. https://doi.org/10.1109/TTE.2022.3183074.
15. Shen, Q.; Cheng, J.; Guo, D.; Yang, T. Analysis and Suppression of Electromagnetic Vibration Noise of Fractional-Slot Concentrated-Windings Interior PMSMs. *IEEE Trans. Transp. Electrif.* **2024**, *10*, 5270–5281. https://doi.org/10.1109/TTE.2023.3330168.
16. Ma, C.; Xu, W.; Liu, M.; Hong, J. Low Vibration Control Scheme for Permanent Magnet Motor Based on Resonance Controllers. *Energies* **2024**, *17*, 4666. https://doi.org/10.3390/en17184666.
17. Xing, Z.; Wang, X.; Zhao, W.; Li, X.; Xiong, L.; Zhang, X. Optimization Design of Interior Permanent Magnet Synchronous Motor with U-Shaped Rotor for Low-Level Torque Ripple and Electromagnetic Vibration. *IEEE Trans. Transp. Electrif.* **2024**, *10*, 1995–2007. https://doi.org/10.1109/TTE.2023.3288892.

18. Yao, L.; Shen, J.X.; Wang, Y.; Shi, D. Fast Prediction and Staged Optimization of Electromagnetic Vibration in Permanent Magnet Synchronous Motor. *IEEE Trans. Ind. Electron.* **2024**, *71*, 115–125. https://doi.org/10.1109/TIE.2023.3250755.
19. Qu, C.; Guo, Z.; Hu, Y.; Wang, X.; Han, F. Multi-Objective Optimization Design of a New Permanent Magnet Synchronous Motor Based on the Taguchi Method. *Energies* **2022**, *15*, 7347. https://doi.org/10.3390/en15197347.
20. Zhang, Y.; Yang, Y.; Gu, Z.Y.; Li, L.; Ma, T. Multi-Objective Optimization for Noise Reduction of IPMSM Based on Non-Uniform Air Gap. *IEEE Access* **2024**, *12*, 48819–48829. https://doi.org/10.1109/ACCESS.2024.3381776.
21. Li, R.; Cao, J.; Li, D.; He, X.; Liu, R. A Novel Rotor Structure with Single Pole-Pair Double-Layer PM Shift to Reduce Torque Ripple and Vibration in Delta-Type IPMSM. *IEEE Trans. Transp. Electrif.* **2026**, *early access*. https://doi.org/10.1109/TTE.2026.3710222.
22. Sato, T.; Watanabe, K.; Igarashi, H. Multimaterial Topology Optimization of Electric Machines Based on Normalized Gaussian Network. *IEEE Trans. Magn.* **2015**, *51*, 7202604. https://doi.org/10.1109/TMAG.2014.2359972.
23. Kim, H.-J.; Lim, D.-K. Topology Optimization of the IPMSM for HEVs Using a Normalized Gaussian Network With Divided Region Method for Weighting Coefficients. *IEEE Access* **2024**, *12*, 170677–170687. https://doi.org/10.1109/ACCESS.2024.3498333.
24. Takenouchi, K.; Hiruma, S.; Mifune, T.; Matsuo, T. Topology and parameter optimization of IPM motor considering mechanical strength by stress and connection constraints. *COMPEL* **2024**, *43*, 839–851. https://doi.org/10.1108/COMPEL-11-2023-0551.

Disclaimer/Publisher's Note: The statements, opinions and data contained in all publications are solely those of the individual author(s) and contributor(s) and not of MDPI and/or the editor(s). MDPI and/or the editor(s) disclaim responsibility for any injury to people or property resulting from any ideas, methods, instructions or products referred to in the content.